

Why Is North Tropical Atlantic SST Variability Stronger in Boreal Spring?

ARNAUD CZAJA

Department of Earth, Atmospheric, and Planetary Sciences, Massachusetts Institute of Technology, Cambridge, Massachusetts

(Manuscript received 17 September 2003, in final form 13 February 2004)

ABSTRACT

It is suggested that the seasonal dependence of interannual variability displayed by observed sea surface temperature (SST) over the north tropical Atlantic primarily reflects the seasonality of the remote forcing associated with the North Atlantic and Southern Oscillations and is controlled by the mean damping time scale of SST anomaly. A stochastic model including a seasonally dependent forcing is used to test this hypothesis against observations.

1. Introduction

A striking feature of interannual climate variability in the tropical Atlantic is its dependence upon the seasons. Figure 1 illustrates this point by displaying the seasonal cycle of interannual variance of key sea surface temperature (SST) indices: the north tropical Atlantic (NTA: 5°–25°N, 60°–20°W), the south tropical Atlantic (STA: 25°S–3°N, 30°W–10°E), and their difference, the interhemispheric SST gradient. One observes weaker year-to-year variations during August–September–October (ASO) for all three indices (all groups of months will hereafter be denoted by their first letters) and stronger year-to-year variations in boreal spring (MAM) for the interhemispheric SST gradient and the “North Tropical Atlantic” index. These relative changes of variance are the largest for the NTA – SST index, for which they amount to about 30% [as measured, from Fig. 1 by the ratio (maximum – minimum)/twice the annual mean].

To some extent, a seasonal dependence of the interannual variability is not unexpected because of large seasonal changes in the mean state of the tropical Atlantic ocean–atmosphere system. For instance, interannual fluctuations of the east–west SST difference along the equator in the Atlantic are mostly seen at the time when the climatological cold tongue is developed, that is, in late summer (e.g., Sutton et al. 2000). Since such fluctuations are believed to reflect large-scale ocean–atmosphere interactions in the equatorial Atlantic

akin to El Niño and the Southern Oscillation (Zebiak 1993), it is likely that the seasonality of the so-called Atlantic Niño mode is induced by local ocean–atmosphere coupling. Here we propose an alternative mechanism for off-equatorial regions, namely that the seasonality seen in SST in Fig. 1 largely reflects the seasonality of remote forcing impacting the tropical Atlantic. We focus on the NTA, which contributes most to the interhemispheric SST gradient seasonality (Fig. 1).

In a recent study (Czaja et al. 2002, hereafter CVM), we showed that the bulk of the interannual variations of NTA SST could quantitatively be understood as a local response of the ocean mixed layer to changes in evaporation induced by the North Atlantic Oscillation (NAO) and ENSO. A simple model for the NTA SST anomaly (T') was put forward as

$$\rho C_p h_0 \frac{dT'}{dt} = F'_{\text{lat}} = G' - \gamma T', \quad (1)$$

where ρ and C_p are, respectively, the density and heat capacity of seawater, h_0 is the annual mean mixed layer depth, and F'_{lat} is the anomalous surface latent heat flux (all variables are spatially averaged over the NTA region and primes stand for departures from the mean seasonal cycle); F'_{lat} was further decomposed into a part G' driven by NAO and ENSO variability (wind-induced changes) and a sensitivity to SST $\gamma T'$ reflecting the local thermodynamic adjustment of the atmosphere to NTA SST anomalies.¹ As both NAO and ENSO variability are strongly dependent upon the seasonal cycle, there is a source of seasonal dependence for T' in the model (1)

Corresponding author address: Dr. Arnaud Czaja, Department of Earth, Ocean, and Planetary Sciences, Massachusetts Institute of Technology, Rm. 54-1517, 77 Massachusetts Avenue, Cambridge, MA 02139.
E-mail: czaja@ocean.mit.edu

¹ Note that we found in CVM very little evidence for a dynamical response of the atmosphere to the NTA SST anomaly *over* the NTA region. This does not exclude the possibility of a larger impact of the NTA SST anomaly on the atmosphere *closer* to the equator.

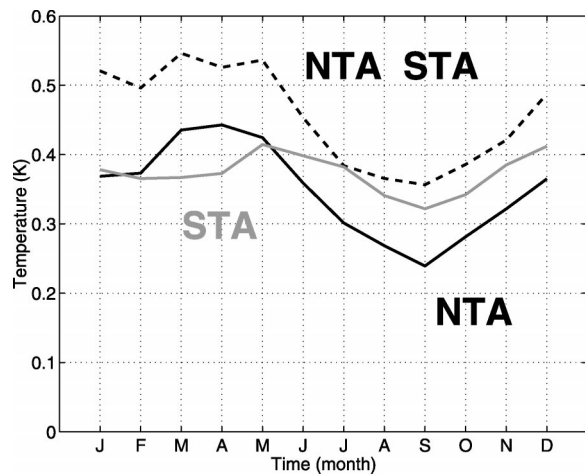


FIG. 1. Interannual variability of SST indices (std dev in K; gray for STA, continuous black for NTA, and dashed black for their difference) for each calendar month, as computed from monthly SST time series from the NCEP–NCAR reanalysis during the period 1960–2002.

through G' . It is the purpose of this paper to test whether the seasonality of NAO and ENSO variability can explain the seasonality observed in NTA SST. We emphasize that the focus of this study is on how the amplitude of interannual SST variability varies among season, which we refer to in the following as the *relative amplitude* of the seasonal cycle of SST variance. The absolute amplitude of NTA SST variability was the focus of CVM.

First, evidence for a strong seasonality of NAO and ENSO impact on sea level pressure gradient and surface evaporation over the NTA region is presented in section 2 using data from the National Centers for Environmental Prediction–National Center for Atmospheric Research (NCEP–NCAR) reanalysis (Kalnay et al. 1996) during the period 1950–99.² The response of T' to a seasonally varying stochastic forcing G' in the model (1) is then studied and compared to observations in section 3. A discussion and conclusions are offered in sections 4 and 5, respectively.

2. Seasonal dependence of NAO and ENSO impact on NTA

a. Sea level pressure

Figure 2 (contours) displays correlation maps of seasonal SLP anomalies over a tropical domain (20°S – 40°N) with a seasonal midlatitude NAO index from Hurrell (see online at <http://www.cgd.ucar.edu/~jhurrell/>

nao/pc.html).³ For each season, we find the largest positive correlations around 30°N , indicative of anomalous northward pressure gradient over the NTA and a corresponding strengthening of the northeast trades in a positive NAO phase. The typical amplitude of the SLP fluctuations (shading) is largest in DJF and MAM and weakest in JJA and SON. Through geostrophic balance, we thus expect a stronger impact of NAO on NTA surface winds during boreal winter and spring than during boreal summer and fall.

Figure 3 is the analog of Fig. 2 but based on a seasonal ENSO index (SST averaged over 5°S – 5°N , 90° – 150°W , i.e., the so-called Niño-3 SST index). The shape of the correlation maps (contours) changes as a function of season somewhat more than in Fig. 2. We observe a northwest–southeast-oriented SLP dipole in DJF and MAM but anticyclonic centers on the poleward flanks of the intertropical convergence zone (ITCZ) in JJA and SON. As in Fig. 2, however, the amplitude of the SLP fluctuations (shading) is largest in boreal winter. The orientation of the SLP dipole in DJF and MAM leads to an efficient modulation of the strength of the northeast trades. In JJA and SON, however, the SLP pattern shows a maximum over the NTA region. As a consequence, we expect weak changes in surface winds induced by ENSO over the NTA region in boreal summer and fall.

The seasonal dependence of the NAO SLP anomalies likely reflects the annual changes in the equator to pole temperature difference, with more active synoptic eddies and low-frequency variability in the atmosphere in boreal winter when the temperature difference is the largest. The mechanisms responsible for the seasonality in the ENSO teleconnection over the tropical Atlantic are less clear. They might involve a response of the seasonal cycle of convection over the tropical Atlantic to the anomalous warming/cooling of the free troposphere in ENSO events (Chiang and Sobel 2002), but also Rossby wave-type teleconnections (i.e., the Pacific–North American pattern) forced from the tropical Pacific and able to reach the North Atlantic subtropics in boreal winter (e.g., Nobre and Shukla 1996).

We now turn to the time domain and investigate the temporal behavior of the SLP patterns shown in Figs. 2 and 3. If NAO variability is known to be associated with a rather short decorrelation time scale (about 10 days; see, e.g., Feldstein 2000), anomalous ENSO events persist for more than a year (e.g., Rasmusson and Carpenter 1982). We thus expect significant differences between the time scale associated with the patterns in Figs. 2 and 3. To address this issue, we have computed the autocorrelation function of a monthly time series of the NAO and ENSO SLP patterns, the time series being

² A linear trend has been removed from all monthly anomaly time series (departure from the mean seasonal cycle) considered in the paper.

³ The index was constructed from a principal component analysis of seasonally averaged SLP anomaly over the North Atlantic sector (20° – 70°N , 90°W – 40°E). The associated patterns (the EOFs) vary in strength and orientation with seasons, while still keeping the familiar dipolar shape.

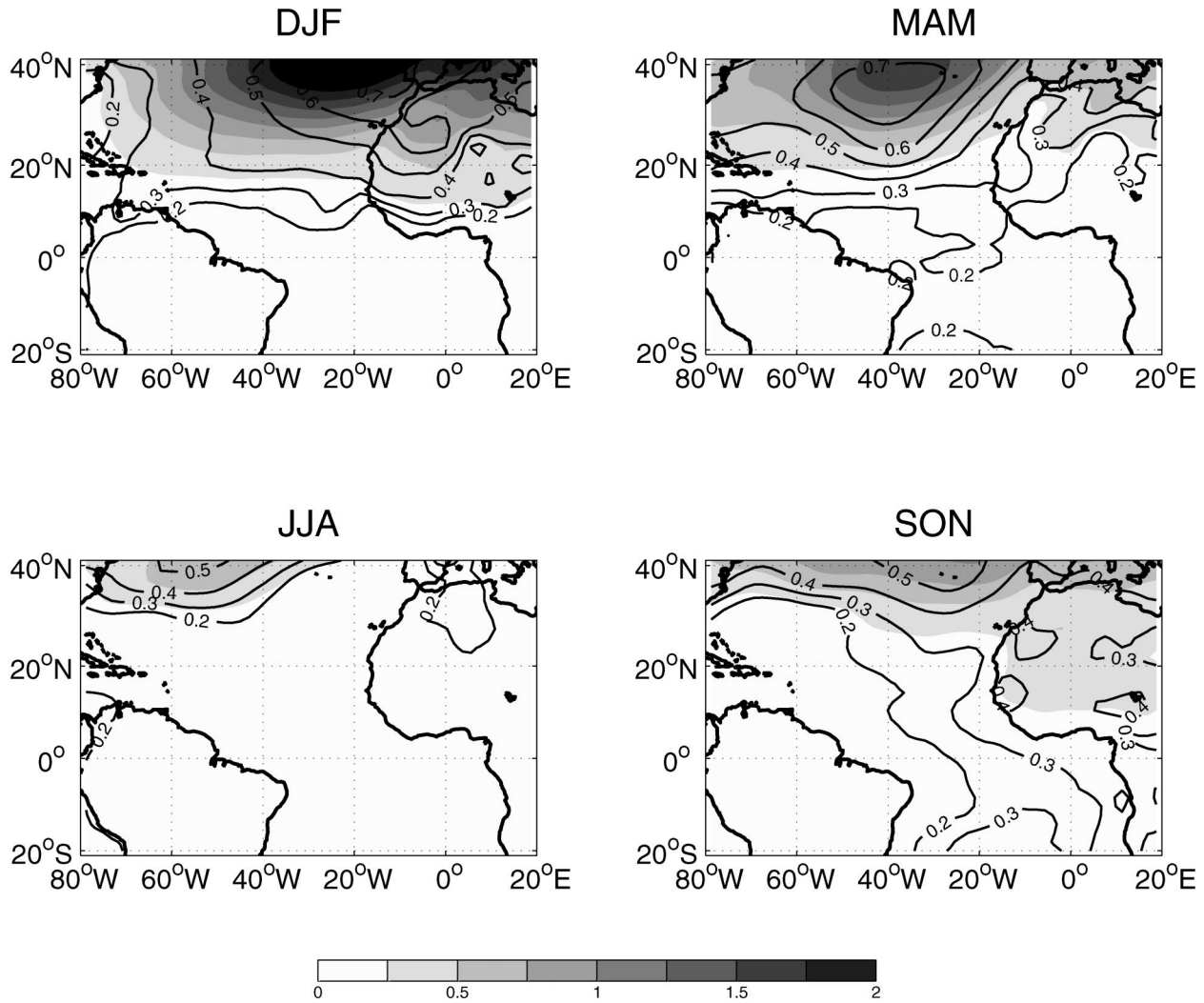


FIG. 2. Simultaneous correlation map of seasonal (3-month average) SLP anomaly and NAO index. The seasons are indicated on the plot. Correlations are drawn as continuous lines when positive (dashed when negative) and are only shown when larger in magnitude than 0.2 with a contour interval of 0.1. Shadings indicate the corresponding amplitude of the SLP fluctuations (in mb, as indicated on the shading scale at the bottom).

obtained by linear regression of the monthly SLP anomaly onto the seasonal SLP patterns of Figs. 2 and 3.⁴ The resulting autocorrelation functions are shown in Fig. 4 as circled broken curves for NAO (left, in black) and ENSO (right, in gray). For NAO, we observe a simple decay as a function of lag τ , which is well fitted by an exponential $e^{-\nu|\tau|}$ with $\nu^{-1} = 19$ days (left, black continuous curve). This is consistent with the midlatitude origin of the NAO and its inherent randomness.

⁴ We start by constructing a December, or January, or February time series by projecting the DJF pattern in Fig. 2 onto the December, or January, or February SLP anomaly matrix over the domain shown in Fig. 2 (20°S–40°N, 80°W–20°E). Then we construct the monthly time series by applying the former procedure to other seasons and “assembling” together the January, February, March, . . . , December time series.

Note that the somewhat long time scale of 19 days found here is likely to reflect the use of monthly data rather than being a true estimate of the NAO decorrelation time scale. Using daily data and upper-level geopotential height, Feldstein (2000) found $\nu^{-1} \approx 9.5$ days.

The ENSO curve on the right-hand side in Fig. 4 is more complex and shows two different time scales: first, a rapid decorrelation after 1 month, which is well captured by an exponential with a similar decorrelation time as NAO ($\nu^{-1} = 25$ days, continuous curve), and second, a slower decay, with correlations falling within an envelope defined by two exponentials $\nu^{-1} = 2$ months and $\nu^{-1} = 3$ months. If one restricts the computation of the 1-month-lag autocorrelation to wintertime months, then its value is similar to that shown in Fig. 4 for NAO (≈ 0.2). If, however, one only considers summertime months, then the 1-month-lag autocorrelation increases

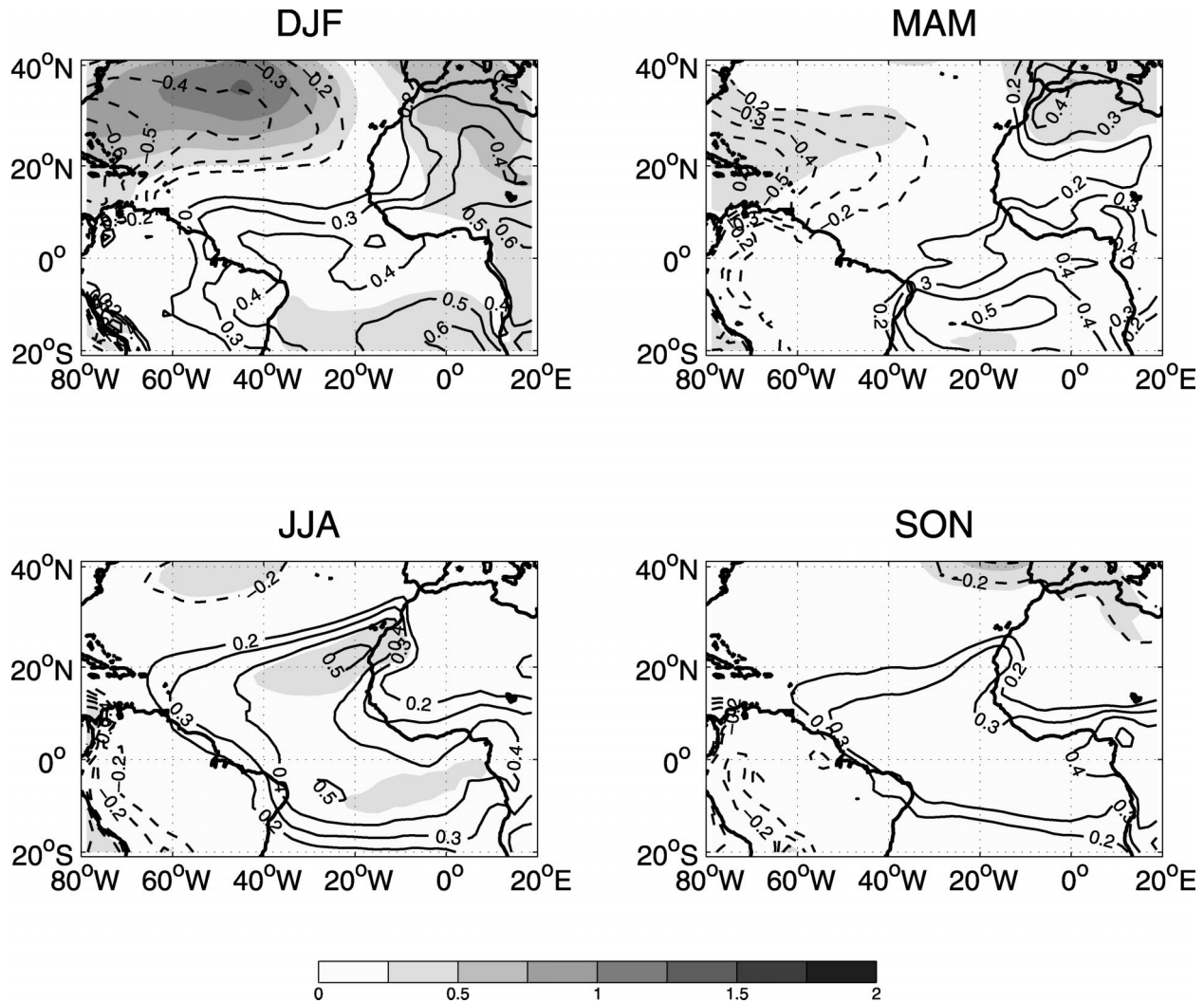


FIG. 3. As in Fig. 2, but based on a seasonal ENSO index.

to ≈ 0.5 . Thus, the two time scales likely reflect the different SLP patterns found in Fig. 3 in DJF and JJA, which are mixed in our procedure by only considering a single time series.

In summary, the ENSO–SLP teleconnection over the tropical Atlantic consists of an energetic (in the sense of the largest amplitude of SLP anomaly in Fig. 3) and rapidly decorrelated pattern in winter. It is expected to drive significant surface wind changes over the NTA region during that season. In summer, however, the ENSO–SLP teleconnection is weaker and more persistent. It should have little impact on surface winds over the NTA region because the latter is precisely where the teleconnection shows SLP extrema. The NAO–SLP teleconnection over the tropical Atlantic essentially keeps the same spatial pattern and time scale along the course of a year. It is strongest in boreal winter and weakest in boreal summer.

b. Surface evaporation

The above analysis suggests a larger impact of ENSO and NAO on the NTA SLP gradient and thus surface winds in boreal winter and spring than in boreal summer and fall. To estimate quantitatively the effect of this seasonality on surface evaporation over the NTA region, we first compute the change in surface wind speed $|w|'$ associated with NAO and ENSO. To do this, we linearly regress monthly wind speed anomalies $|w|'$ (averaged over the NTA region) onto the monthly time series of the NAO and ENSO SLP patterns used in Fig. 4. In this way, a statistical model is used to link changes in SLP gradient and surface wind speed.

Figure 5 displays the resulting seasonal evolution of $|w|'$ for NAO (black) and ENSO (gray, with signs reversed for easier comparison with NAO). Anomalously high wind speed occurs in DJF of positive NAO/neg-

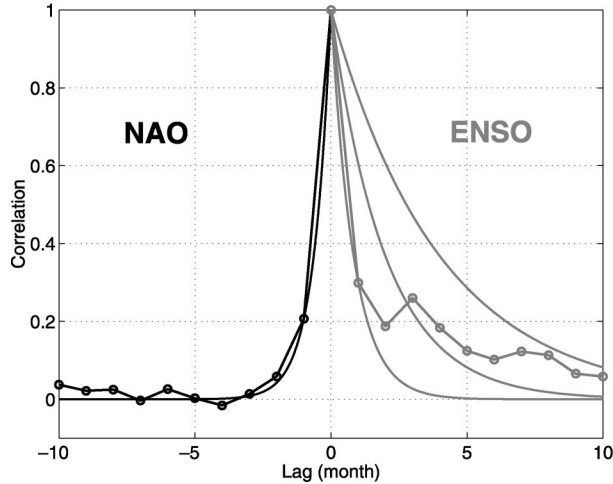


FIG. 4. Autocorrelation function of monthly NTA SLP index associated with NAO (broken black on the left) and ENSO (broken gray on the right). The lag is in months, and since the autocorrelation function is symmetric with respect to lag, only one side is shown (negative lags for NAO, positive lags for ENSO). Some useful exponential curves are superimposed as continuous lines.

ative ENSO years, consistent with the stronger northward pressure gradient during these winters (Figs. 2, 3). Only weak wind speed anomalies occur in JJA of positive NAO/negative ENSO years, reflecting the weak anomalous SLP gradient found during that time (Figs. 2 and 3). The amplitude of the seasonal changes ranges from $\approx 0.5 \text{ m s}^{-1}$ to essentially zero.

We then estimate the wind-induced change in latent heat flux F'_{lat} [i.e., G' in Eq. (1)] associated with ENSO and NAO SLP patterns, according to

$$G' \equiv \left(\frac{\partial F'_{\text{lat}}}{\partial |w|'} \right)_{T=0} |w|' = L_v \rho_a C_E (\bar{q}_a - \bar{q}_s) |w|', \quad (2)$$

where L_v is the latent heat of vaporization, ρ_a the air density, $C_E = 1.5 \times 10^{-3}$ a drag coefficient, q_s the saturation specific humidity at SST, and q_a the specific humidity 2 m above ground. All variables in (2) are averaged over the NTA region and vary according to a monthly climatology (denoted by an overbar)⁵ except for $|w|'$, which was estimated by linear regression (Fig. 5).

Figure 6 displays G' for NAO (black) and ENSO (gray), where, to make the comparison clear with Fig. 5, we now have reversed the sign of the NAO curve. In so doing, it is seen that for all seasons, positive ENSO/negative NAO conditions induce an anomalous surface warming of the NTA region through changes in surface wind speed. The phase of the seasonal variations in G' are very similar to that of $|w|'$ (Fig. 5), with a larger anomaly in DJF and very little variability during

⁵ Almost identical results are found if the product $(\bar{q}_s - \bar{q}_a) |w|'$ is first computed for each grid point and then all grid points of the NTA region averaged together.

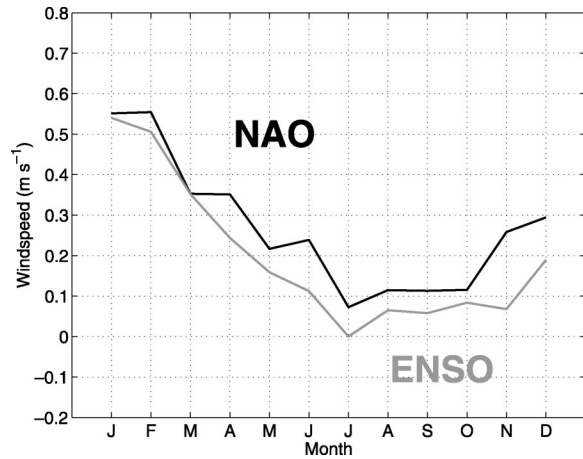


FIG. 5. Wind speed anomaly $|w|'$ (in m s^{-1}) over the NTA region associated with the seasonally varying NAO (black) and ENSO (gray) SLP indices. The value gives the typical change in wind speed associated with one std dev of the SLP index.

boreal summer and fall. Actually, Fig. 6 is almost unchanged if one uses the annual average of $\bar{q}_s - \bar{q}_a$ rather than its monthly value (not shown). One reason for this is that the SST averaged over the NTA region has only moderate seasonal mean variations (about 2–3 K). Assuming a fixed relative humidity of 0.8 above the sea surface, the seasonal variations in $(\bar{q}_s - \bar{q}_a)$ expected from the seasonal changes in SST, computed from the Clausius–Clapeyron relationship, are only of order 15%. Although they tend to damp the seasonal variations in G' [colder mean SST in JFM, warmer mean SST in ASO—not shown], they are not sufficiently large to make a difference in (2). Overall, Fig. 6 is a mirror image of Fig. 5, and the seasonal variations in G' (from ≈ 10 to $0\text{--}2 \text{ W m}^{-2}$) essentially reflect those of $|w|'$ and a mean sensitivity $\partial F'_{\text{lat}} / \partial |w|' \approx -20 \text{ W m}^{-2} (\text{m s}^{-1})^{-1}$.

We thus come to a very simple picture in which the

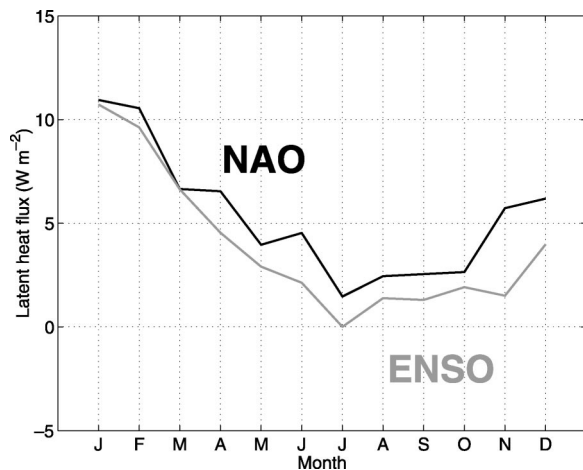


FIG. 6. As in Fig. 5 but for wind-induced changes in latent heat flux (in W m^{-2}), i.e., typical values of G' in (1).

seasonality in ENSO and NAO teleconnections drives a seasonality in surface evaporation over the NTA region, which is that of the surface wind speed anomaly and is not altered by the mean seasonal cycle. We now investigate if this forcing alone can account for the seasonal variations seen in NTA SST in Fig. 1.

3. Seasonal dependence of NTA SST variability

Let us rewrite (1) as

$$\frac{dT'}{dt} = F' - \lambda T', \quad (3)$$

where $\lambda = \gamma/\rho C_p h_0$ is an inverse oceanic damping time scale (about 6 months for NTA SST; see CVM) and $F' = G'/\rho C_p h_0$. For a stochastic forcing F' with an annual cycle of variance, one expects that, if λ is very small (long damping time scale), T' and F' will be in quadrature, meaning that the maximum in T' variance will lag that of F' by $12/4 = 3$ months. On the other hand, if λ is very strong (short damping time scale), then $F' \approx \lambda T'$ and T' and F' should have the same annual cycle in both amplitude and phase.

To assess which regime is relevant to the north tropical Atlantic region, we have solved (3) for a forcing F' with autocovariance at a lag τ given by (brackets denote an ensemble average)

$$\langle F'(t)F'(t + \tau) \rangle = \sigma^2 e^{-\nu|\tau|} (1 + a \cos \omega_a t). \quad (4)$$

This choice is motivated by section 2 and is to be taken as the simplest stochastic model for both NAO and ENSO forcings, including an inverse decorrelation time scale ν and a variance being a function of season. The seasonal dependence is represented by a single harmonic at the annual pulsation ω_a with a relative amplitude $a \approx 1$, as suggested in Fig. 6. The parameter σ^2 measures the annual mean variance of the forcing. Note that because the model (3) is linear, we decompose the NTA SST anomaly response T' as a sum of the separate response to ENSO (T'_1) and NAO (T'_2) forcings (F'_1 and F'_2 , respectively, with parameters $a_1, a_2, \nu_1, \nu_2, \sigma_1, \sigma_2$) satisfying $dT'_1/dt = F'_1 - \lambda T'_1$ and $dT'_2/dt = F'_2 - \lambda T'_2$. Since NAO and ENSO are essentially independent modes of variability, $\langle T'(t)T'(t + \tau) \rangle = \langle T'_1(t)T'_1(t + \tau) \rangle + \langle T'_2(t)T'_2(t + \tau) \rangle$.

The choice of inverse decorrelation time scales ν_1, ν_2 requires further discussion. It was shown in section 2a that the temporal behavior of the NAO teleconnection over the tropical Atlantic can be reasonably simulated by taking $\nu_2^{-1} \approx 3$ weeks. That of the ENSO teleconnection showed more complexity, as for instance a dependence of ν on the season, which is not modeled by (4). Since, however, the ENSO teleconnection over the NTA has only a very weak impact on surface evaporation in the summer (Fig. 6) and behaves very similarly to the NAO teleconnection during winter, a simple choice for ν_1 is to take $\nu_1^{-1} = \nu_2^{-1} = \nu^{-1} = 3$ weeks. As mentioned in section 2a, the precise estimation of ν

would require daily data, and a choice of 3 weeks is to be taken just as a placeholder. As shown in the appendix, the model prediction is not sensitive to the particular choice of ν , as long as it remains short compared to the annual period.

The computation of the SST autocovariance from (3) and (4) is tedious and left to the appendix. Nevertheless, a useful approximation to the full solution can be found by considering the limit in which the ENSO and NAO decorrelation time scale ν^{-1} is short compared to both the annual cycle and the SST damping time scale. If one further uses the same parameters for ENSO and NAO [i.e., (i) same temporal phase, (ii) $a_1 = a_2 = a$, (iii) $\sigma_1 = \sigma_2 = \sigma$ —all suggested in Fig. 6], a prediction for the SST variance reads

$$\begin{aligned} \langle T'(t)T'(t + \tau) \rangle \approx & \frac{2\sigma^2}{\lambda\nu} \left[1 + a \frac{(2\lambda/\omega_a)}{1 + (2\lambda/\omega_a)^2} \right. \\ & \left. \times \left(\frac{2\lambda}{\omega_a} \cos \omega_a t + \sin \omega_a t \right) \right]. \end{aligned} \quad (5)$$

Equation (5) shows that the relative amplitude and phase of the annual cycle of SST variance is controlled by one single parameter, the ratio R of annual period and SST damping time scale:

$$R \equiv \frac{2\lambda}{\omega_a}. \quad (6)$$

When $R \gg 1$, one recovers the result that T' and F' have the same annual cycle of variance in phase and relative amplitude, the SST variance behaving like $1 + a \cos \omega_a t$. When $R \ll 1$, T' and F' are in phase quadrature (3-month lag) and the relative amplitude of the seasonal cycle in T' becomes very weak, the SST variance behaving like $1 + Ra \sin \omega_a t$. In this regime, the persistence time of the SST anomaly (λ^{-1}) is so much longer than a year that the seasonality of the stochastic forcing amplitude makes no difference.

Figure 7 illustrates the approximate and full solution for SST (dashed and continuous black curves, respectively), to which is superimposed the annual cycle of the forcing, that is, F' (gray). To produce these, parameters were set to $a = 0.95$ and $\lambda^{-1} = 6$ months ($R \approx 0.6$). The phase of the forcing was set to reach a maximum in January. Note that for easier comparison with Figs. 1 and 6, the standard deviation, not the variance, is shown. All curves are nondimensional since, as introduced in section 1, we focus on the relative changes of SST anomaly amplitude between seasons.

A striking feature of the model prediction is that the seasonal dependence of SST is significantly reduced compared to that of the forcing. This is consistent with observations, as Fig. 6 indicates $O(1)$ magnitude changes for F'_{lat} , but Fig. 1 indicates only 30% changes in NTA SST. This number is consistent with that predicted

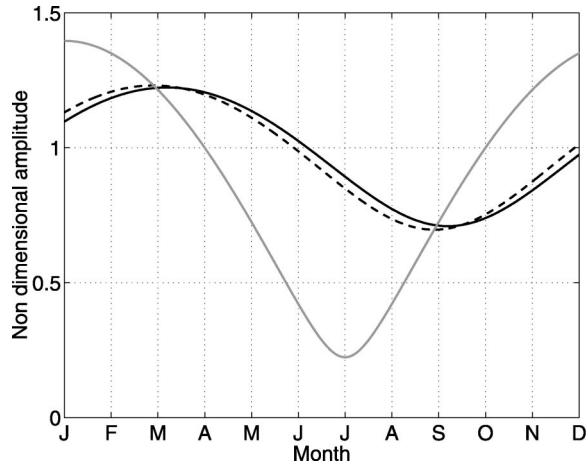


FIG. 7. Nondimensional std dev of the model forcing F' (gray) and SST anomaly as a function of calendar month (black curves; continuous for the full prediction, dashed for the approximate solution).

by the model. In addition, we observe in Fig. 7 that the maximum (minimum) SST anomaly amplitude is found about 2 months after that of the forcing, that is, in March–April (September–October). Again, this is in good agreement with Fig. 1. Both of these results (phase and amplitude of the seasonality) reflect that the damping time scale of the SST anomaly is close to the annual period, so the regime relevant to the tropical Atlantic is an intermediate one, that in which $R \approx 1$.

4. Discussion

The zero-order model (1) contains other sources of seasonal dependence than simply that of the forcing G' . Indeed, both the mixed layer depth h_0 and the sensitivity of latent heat flux to SST γ undergo seasonal variations. The climatology of Levitus and Boyer (1994) indicates that h_0 reaches its maximum value (~ 50 m) in JFM and its minimum value (~ 25 m) from June to October. The seasonal variations in h_0 (30%) are thus weaker than those estimated for G' (about 100%—see Fig. 6) but are not insignificant. Since G' has maximum (minimum) strength in boreal winter (summer)—see Fig. 6—seasonal variations in h_0 tend to weaken the seasonality in the overall forcing $F' = G'/\rho C_p h_0$. This buffering effect has actually been taken into account when constructing Fig. 7 by setting the relative amplitude of F' (gray curve) to be about 30% smaller than observed (Fig. 6).

The seasonality in γ is more difficult to estimate, but Frankignoul and Kestenare (2002) suggest slightly stronger γ ($\sim 13 \text{ W m}^{-2} \text{ K}^{-1}$) in boreal winter and spring and slightly weaker γ ($\sim 9 \text{ W m}^{-2} \text{ K}^{-1}$) in boreal summer and fall. These variations (about 20%) are again buffered by those of h_0 , yielding seasonal variations in λ of about 10% ($\delta\lambda/\lambda = \delta h_0/h_0 - \delta\gamma/\gamma \approx 0.3 - 0.2 = 0.1$), thus of secondary importance compared to those of G' . It is nevertheless a useful check to estimate, when no seasonality in G' is allowed, what is the seasonality

of λ needed to reproduce the observations. Analytical calculations are still possible but become even more arduous [see Ruiz de Elvira and Lemke (1982) for the case of white noise forcing G'], so we simply carried out numerical simulations. Physically, one expects that seasons when the damping rate is larger (smaller) will be associated with weaker (stronger) SST anomaly, allowing for some lag due to SST persistence. The numerical experiments showed that to reproduce the observed seasonal dependence of SST anomaly variance, λ needs to have seasonal variations of at least 50% and needs to be weaker a few months before boreal spring and stronger a few months before summer. This phasing is roughly consistent with that associated with h_0 (assuming the seasonal variations of h_0 dominate those of γ , as suggested above) but the required amplitude ($>50\%$) is too strong compared to our estimate of $\delta\lambda/\lambda \approx 10\%$. This reinforces our conclusion that the main source of seasonality in (1) is G' .

It needs to be emphasized that we have assumed that the model (1) holds for each season, and this should be justified. CVM made a careful analysis of the mixed layer heat budget over the NTA region in boreal spring and found clear indication that evaporation balances the tendency term and dominates over changes in sensible and radiative heating during that season. But what about other seasons? Further analysis of the interannual variability of sensible and radiative heating over the NTA region confirmed the dominance of changes in evaporation during seasons other than boreal spring (not shown). Evaporation changes were found to be larger than either sensible or radiative heating by a factor ranging from 2–3 in JJA to 4 in DJF. No significant seasonal dependence of the interannual variability of either sensible or radiative heating could be found. This clearly gives support for the use of (1) for all seasons and emphasizes the dominant role of evaporation being responsible for the seasonality seen in NTA SST.

Finally, one remaining issue is whether, as we argued, the changes in evaporation can solely be attributed to local changes in wind speed and SST. Changes in humidity of the atmospheric boundary layer could indeed also play a role (e.g., Chiang and Sobel 2002), but they could be incorporated into the model (1) through an additional forcing term correlated with G' . Bulk-formula estimates and the simple model developed in section 3 seem, however, to suggest that this is not needed.

5. Conclusions

Despite its simplicity, the zero-order model (1) provides a plausible explanation for the observed fact that NTA SST anomalies show largest (weakest) year-to-year variations in boreal spring (early fall). The phase and amplitude of this seasonality reflect primarily that of the remote forcing by NAO and ENSO, but also the strength of local ocean–atmosphere coupling. Indeed, the relevant parameter of the model (1) is the ratio R

of the annual period to the damping time scale of SST anomaly, the latter being largely controlled by local air–sea interactions for the NTA region (see CVM). Were the coupling much weaker (shorter damping time scale, $R \gg 1$), the relative amplitude of the seasonal cycle of SST variance would be larger and would be in phase with that of the NAO and ENSO forcing. Conversely, if the coupling was much stronger (longer damping time scale, $R \ll 1$), one would observe essentially no seasonal dependence of SST variance upon the season.

It is emphasized that the validity of these results is certainly restricted to north tropical Atlantic SST. It is very likely that the interannual variability of the position and strength of the Atlantic ITCZ is more sensitive to the seasonality of local ocean–atmosphere coupling and less sensitive to the seasonality of the remote forcing (Chiang et al. 2002). This is currently under study.

Acknowledgments. The author was supported by a grant from the CLIVAR Atlantic Program of the Office of Global Programs of the National Oceanic and Atmospheric Administration. The comments of two anonymous reviewers and J. Marshall were very helpful.

APPENDIX

Prediction of the SST Variance

The general solution of (3) is written as

$$T'(t) = e^{-\lambda t} \int_{-\infty}^t F'(s)e^{\lambda s} ds + T'(t = 0)e^{-\lambda t}. \quad (A1)$$

Since the variance $\sigma_T^2(t) = \langle T'(t)T'(t) \rangle$ should not depend on the initial condition $T'(t = 0)$, it is only determined by the contribution of the first term on the rhs of (A1), namely,

$$\begin{aligned} \sigma_T^2(t) &= \left\langle \left[e^{-\lambda t} \int_{-\infty}^t F'(s)e^{\lambda s} ds \right]^2 \right\rangle \\ &= e^{-2\lambda t} \int_{-\infty}^t \int_{-\infty}^t \langle F'(r)F'(s) \rangle e^{\lambda(s+r)} ds dr, \quad (A2) \end{aligned}$$

where the angle brackets denote an ensemble average. Ruiz de Elvira and Lemke (1982) solved (A2) for a white noise forcing $\langle F'(r)F'(s) \rangle = \delta(r - s)(1 + a \cos \omega_a s)$, but because of the month-to-month persistence seen in Fig. 4, we want to solve instead for $\langle F'(r)F'(s) \rangle = \sigma^2 e^{-\nu|r-s|}(1 + a \cos \omega_a s)$, as in (4). Defining a new variable $z = s - r$, Eq. (A2) is rewritten as

$$\begin{aligned} \sigma_T^2(t) &= \sigma^2 e^{-2\lambda t} \int_{-\infty}^t \int_{-\infty}^{t-r} [1 + a \cos \omega_a(z + r)] \\ &\quad \times e^{-\nu|z|} e^{\lambda(z+2r)} dz dr, \quad (A3) \end{aligned}$$

which, after integrations over two subdomains ($z \leq 0, r \leq t$) and ($0 \leq z \leq t - r, r \leq t$), reduces to

$$\sigma_T^2(t) = \frac{\sigma^2}{\lambda(\lambda + \nu)}(1 + A \cos \omega_a t + B \sin \omega_a t), \quad (A4)$$

where

$$A = a \frac{\lambda(\lambda + \nu)}{\omega_a^2 + 4\lambda^2} \left[\frac{2\lambda}{\lambda + \nu} + \frac{2\nu\lambda + 2\lambda^2 - \omega_a^2}{\omega_a^2 + (\lambda + \nu)^2} \right] \quad \text{and} \quad (A5)$$

$$B = a \frac{\lambda(\lambda + \nu)}{\omega_a^2 + 4\lambda^2} \left[\frac{\omega_a}{\lambda + \nu} + \frac{\omega_a(\nu + 3\lambda)}{\omega_a^2 + (\lambda + \nu)^2} \right]. \quad (A6)$$

Defining the nondimensional parameters

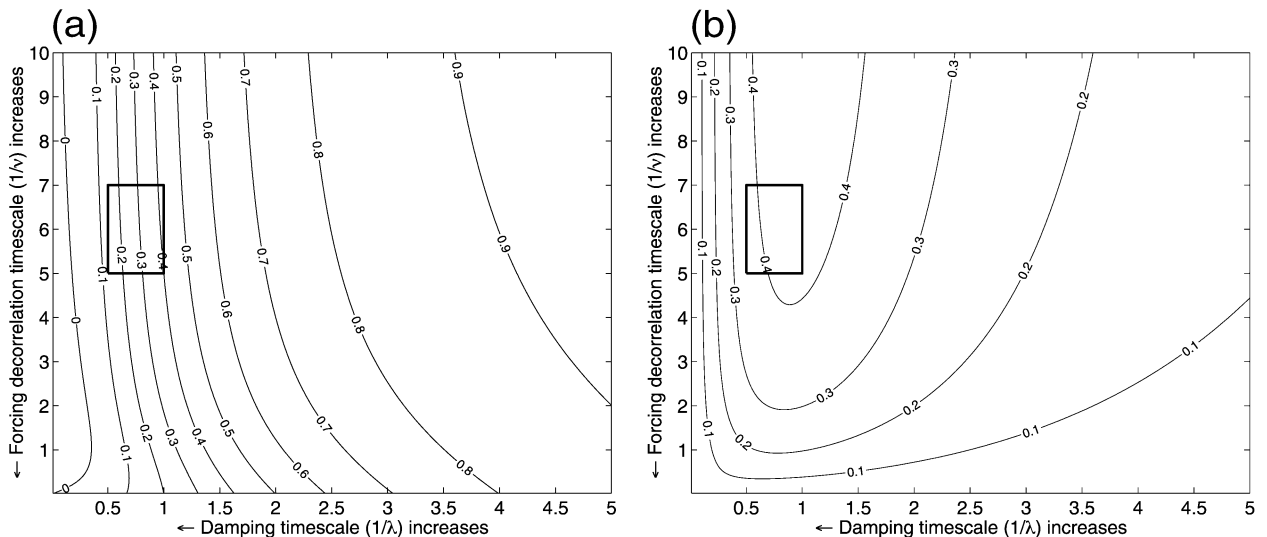


FIG. A1. Contours of (a) A/a and (b) B/a as a function of the nondimensional parameters R (x axis, from 0 to 5) and P (y axis, from 0 to 10). The black box indicates the regime of parameters relevant to NTA SST variability.

$$R \equiv \frac{2\lambda}{\omega_a}, \quad P \equiv \frac{2\nu}{\omega_a}, \quad Q \equiv \frac{P}{R} = \frac{\nu}{\lambda}, \quad (\text{A7})$$

one can rewrite A and B as

$$A = a \frac{R(R+P)}{2(1+R^2)} \left[\frac{1}{1+Q} + \frac{RP+R^2-2}{4+(R+P)^2} \right] \quad \text{and} \quad (\text{A8})$$

$$B = a \frac{RP}{2(1+R^2)} \left[\frac{1}{R+P} + \frac{P+1.5R}{4+(R+P)^2} \right]. \quad (\text{A9})$$

Figures A1a,b display the amplitude factors A and B , respectively, as a function of the inverse damping time scale R (x axis) and the inverse decorrelation time scale P (y axis). As discussed in the main text, the relevant values for NTA SST are found using $\lambda^{-1} \approx 6$ months and $\nu^{-1} \approx 3$ weeks, that is, $R \approx 0.6$, $P \approx 6$, and $Q \approx 10$. This region of parameter is highlighted by a box in Figs. A1a,b.

The general behavior of the curves is well described by taking the asymptotic limit in which $P \gg 1$ and $Q \gg 1$; that is, when the decorrelation time scale of the forcing is shorter than the annual period and the damping time scale. In this limit,

$$A \approx a \frac{R^2}{1+R^2}, \quad B \approx a \frac{R}{1+R^2}. \quad (\text{A10})$$

The last two equations indeed capture the dominance of the in-phase response A for large R , and the slightly greater value of the quadrature-phase response B for $0 \leq R \leq 1$. The maximum value of B close to $R = 1$ in Fig. A1b is also predicted by the above-simplified expression. Equation (A10) was used to derive (5).

The asymptotic limit $P \gg 1$ and $Q \gg 1$, however, cannot address the dependence of A and B upon the decorrelation time scale ν^{-1} . As seen in Fig. A1, this dependence is very weak for A (Fig. A1a) but becomes significant for B when both $(R, P) \approx 1$ (Fig. A1b, when the contours become horizontal), that is, when both the damping and the forcing decorrelation time scales are close to the annual period. In this regime of parameters, the sensitivity is such that the less (more) persistent the forcing, the stronger (weaker) the quadrature response B .

Stochastic atmospheric forcing over the north tropical Atlantic is persistent much less than a year ($P \approx 6$), so

the regime $(R, P) \approx 1$ is not relevant to the physical situation studied here. This regime could however apply to other subtropical regions and provide a model for the oceanic forcing of SST anomalies through entrainment of anomalous water from below the mixed layer, rather than a model for atmospheric forcing. The stochastic oceanic forcing would then be associated with the undulation of isotherms in the upper thermocline, with a typical time scale of a few years in the subtropics. The seasonality would reflect that the communication between the mixed layer and the thermocline only occurs when the mixed layer is deepening, typically from fall to winter.

REFERENCES

- Chiang, J. C., and A. Sobel, 2002: Tropical tropospheric temperature variations caused by ENSO and their influence on the remote tropical climate. *J. Climate*, **15**, 2616–2631.
- , Y. Kushnir, and A. Giannini, 2002: Deconstructing Atlantic ITCZ variability: Influence of the local cross-equatorial SST gradient and remote forcing from the eastern equatorial Pacific. *J. Geophys. Res.*, **107**, 4004, doi:10.1029/2000JD000307.
- Czaja, A., P. van der Vaart, and J. Marshall, 2002: A diagnostic study of the role of remote forcing in tropical Atlantic variability. *J. Climate*, **15**, 3280–3290.
- Feldstein, S. B., 2000: The timescale, power spectra, and climate noise properties of teleconnection patterns. *J. Climate*, **13**, 4430–4440.
- Frankignoul, C., and E. Kestenare, 2002: The surface heat flux feedback. Part I: Estimates from observations in the Atlantic and North Pacific. *Climate Dyn.*, **19**, 633–647.
- Kalnay, E., and Coauthors, 1996: The NCEP/NCAR 40-Year Reanalysis Project. *Bull. Amer. Meteor. Soc.*, **77**, 437–471.
- Levitus, S., and T. P. Boyer, 1994: *Temperature*. Vol. 4. *World Ocean Atlas 1994*, NOAA Atlas NESDIS 4, 117 pp.
- Nobre, P., and J. Shukla, 1996: Variations in sea surface temperature, wind stress, and rainfall over the tropical Atlantic and South America. *J. Climate*, **9**, 2464–2479.
- Rasmusson, E. M., and T. H. Carpenter, 1982: Variations in tropical sea surface temperature and surface wind fields associated with the Southern Oscillation/El Niño. *Mon. Wea. Rev.*, **110**, 354–384.
- Ruiz de Elvira, A., and P. Lemke, 1982: Langevin equation for stochastic climate models with periodic feedback and forcing variance. *Tellus*, **34**, 313–320.
- Sutton, R. T., S. P. Jewson, and D. P. Rowell, 2000: The elements of climate variability in the tropical Atlantic region. *J. Climate*, **13**, 3261–3284.
- Zebiak, S. E., 1993: Air–sea interaction in the equatorial Atlantic region. *J. Climate*, **6**, 1567–1586.